14. M. E. Raymo, W. F. Ruddiman, J. Backman,
    B. M. Clement, D. G. Martinson, *Paleoceanography* **4**,
    413 (1989).
15. P. A. Martin *et al.*, *Earth Planet. Sci. Lett.* **198**, 193 (2002).
16. H. Elderfield, J. Yu, P. Anand, T. Kiefer, B. Nyland,
    Earth Planet. Sci. Lett. **250**, 633 (2006).
17. J. Yu, H. Elderfield, *Earth Planet. Sci. Lett.* **276**, 129
    (2008).
18. N. J. Shackleton, *Science* **289**, 1897 (2000).
19. E. A. Boyle, L. D. Keigwin, *Earth Planet. Sci. Lett.* **76**, 135
    (1985).
20. M. E. Raymo, B. Grant, M. Horowitz, G. H. Rau,
    Mar. Micropaleontology **27**, 313 (1996).
21. K. T. Lawrence, T. D. Herbert, C. M. Brown, M. E. Raymo,
    A. M. Haywood, Paleoceanography **24**, PA2218, 10.1029/
    2008PA001669 (2009).
22. E. L. McClymont, A. Roselle-Mele, *Geology* **33**, 389 (2005).
23. N. J. Shackleton, *Cent. Natl. Rech. Sci. Colloq. Int.* **219**,
    203 (1974).
24. R. G. Fairbanks, *Nature* **342**, 637 (1989).
25. J.-C. Duplessy, L. Labeyrie, C. Waelbroeck, *Quat. Sci. Rev.*
    21, 315 (2002).
26. M. Mudelsee, M. E. Raymo, *Paleoceanography* **20**,
    10.1029/2005PA001153 (2005).
27. T. M. Cronin *et al.*, *Palaeogeogr. Palaeoclimatol.*
    Palaeoecol. **108**, 437 (1994).
28. A. Kitamura, T. Kawagoe, *Quat. Sci. Rev.* **25**, 323 (2006).
29. D. J. Lunt, G. L. Foster, A. M. Haywood, E. J. Stone, *Nature*
    454, 1102 (2008).
30. R. Bintanja, R. S. W. van de Wal, *Nature* **454**, 869
    (2008).
31. D. A. Hodell, J. E. T. Channell, J. H. Curtis, O. E. Romero,
    U. Rohl, *Paleoceanography* **23**, PA4218, 10.1029/
    2008PA001591 (2008).
32. C. Waelbroeck *et al.*, *Quat. Sci. Rev.* **21**, 295 (2002).
33. M. Siddall *et al.*, *Nature* **423**, 853 (2003).
34. D. W. Lea, P. A. Martin, D. K. Pak, H. J. Spero, *Quat. Sci. Rev.*
    21, 283 (2002).
35. We thank J. Wright for assistance with isotope measurements
    and suggestions, M. Raymo for numerous discussions, and
    W. Zhang and K. Lawrence for assistance with time series
    analysis. Two anonymous reviewers provided insightful
    suggestions that substantially improved the manuscript. We
    acknowledge the ODP and Woods Hole Oceanographic
    Institution Seafloor Samples Laboratory for supplying
    sediment samples. This work was supported by a USSSP
    Schlanger ODP Fellowship to S.S. and NSF award OCE
    02-20922 to Y.R.

Transient Simulation of Last Deglaciation with a New Mechanism for Bølling-Allerød Warming

Z. Liu,[1,2,3]* B. L. Otto-Bliesner,[4] F. He,[3] E. C. Brady,[4] R. Tomas,[4] P. U. Clark,[5] A. E. Carlson,[6] J. Lynch-Stieglitz,[7] W. Curry,[8] E. Brook,[5] D. Erickson,[9] R. Jacob,[10] J. Kutzbach,[3] J. Cheng[1,3]

We conducted the first synchronously coupled atmosphere-ocean general circulation model simulation from the Last Glacial Maximum to the Bølling-Allerød (BA) warming. Our model reproduces several major features of the deglacial climate evolution, suggesting a good agreement in climate sensitivity between the model and observations. In particular, our model simulates the abrupt BA warming as a transient response of the Atlantic meridional overturning circulation (AMOC) to a sudden termination of freshwater discharge to the North Atlantic before the BA. In contrast to previous mechanisms that invoke AMOC multiple equilibrium and Southern Hemisphere climate forcing, we propose that the BA transition is caused by the superposition of climatic responses to the transient CO_2 forcing, the AMOC recovery from Heinrich Event 1, and an AMOC overshoot.

The last deglaciation (~21 to 11 ka) (ka: 1000 years ago) experienced the last major natural global warming and was punctuated by several abrupt climate changes (*1*, *2*). Particularly notable changes occurred in the North Atlantic region where the surface climate experienced cooling during Heinrich Event 1 (H1, ~17 ka), followed by an abrupt warming at the onset of the Bølling-Allerød (BA, ~14.5 ka) (Fig. 1) (*2–11*). These abrupt climate changes were accompanied by large changes in the Atlantic meridional overturning circulation (AMOC), suggesting a causal linkage through the AMOC and its associated heat transport (*5*, *6*) (Fig. 1C).

Climate evolution during the last deglaciation has been studied in transient simulations with climate models of intermediate complexity (*12*). In particular, some intermediate models simulated abrupt warming events like the BA by triggering a resumption of the AMOC either locally by a reduced meltwater flux (MWF) (*13*) or surface warming (*14*) over the North Atlantic, or remotely by an increased MWF (*15*) or surface warming (*16*) over the Southern Ocean. In all the cases, the abrupt warming occurred in response to a gradually varying forcing (*17*) through a strong hysteresis associated with AMOC advection and North Atlantic convection (*18*). Long transient simulations, however, have not been carried out in synchronously coupled atmosphere-ocean general circulation models (CGCMs), which

include the most advanced climate physics and are currently being used for future climate projections. Here we present a transient simulation of the climate evolution from the Last Glacial Maximum (LGM, ~21 ka) to BA using a state-of-art CGCM: the National Center for Atmospheric Research Community Climate System Model version 3 (NCAR CCSM3) (*19*). Through realistic changes in boundary conditions and forcing, our simulation captures many major features of the deglacial climate evolution, including the magnitude of the climate response as inferred from observations.

Starting from a previous LGM simulation (*20*), our model was integrated from 22 toward 14 ka, forced by changes in insolation (*21*), atmospheric greenhouse gas (GHG) concentrations (*22*) (Fig. 1A), continental ice sheets and coastlines (*23*, *24*), and MWF over the North Atlantic and Gulf of Mexico (Materials and Methods 1). From 22 to 19 ka, the model climate changes slowly, primarily due to insolation forcing. The simulated Atlantic Ocean at 19 ka, which we call the glacial state, captures important features of the LGM circulation as reconstructed from various proxy records (*25*, *26*), including a shallower North Atlantic Deep Water (NADW) accompanied by a southward shift of deep convection from the Nordic Seas to the Greenland Sea, a reduced AMOC transport, and a volumetric expansion of Antarctic Bottom Water (Fig. 2, A and D and figs. S1A and S2) (Materials and Methods 1).

From 19 to 17 ka, we applied a MWF derived from Northern Hemisphere ice sheets to the North Atlantic and Gulf of Mexico at a rate consistent (within uncertainties) with the record of sea-level rise (*23*, *27*), gradually reaching a peak flux of 20 m per thousand years (ky) at H1 (Fig. 1, B and C). The MWF was then reduced in two scenarios: a linear decrease to zero at 14.2 ka (DGL-B) and a constant flux (of 15 m/ky) until a sudden shut-off at 14.67 ka (DGL-A) (Materials and Methods 2). Because the meltwater termination scenarios DGL-B and DGL-A represent the slowest and fastest possible MWFs, the two corresponding experiments represent two

[1]Key Laboratory of Meteorological Disaster, Nanjing University of Information Science and Technology, Nanjing, 210044, China. [2]State Key Laboratory of Loess and Quaternary Geology, Institute of Earth Environment, Chinese Academy of Sciences, Xi'an, 710075, China. [3]Center for Climatic Research and Department of Atmospheric and Oceanic Sciences, University of Wisconsin, Madison, WI 53706, USA. [4]Climate and Global Dynamics Division, National Center for Atmospheric Research, Boulder, CO 80307–3000, USA. [5]Department of Geosciences, Oregon State University, Corvallis, OR 97331, USA. [6]Department of Geology and Geophysics and Center for Climatic Research, University of Wisconsin, Madison, WI 53706, USA. [7]School of Earth and Atmospheric Sciences, Georgia Institute of Technology, Atlanta, GA 30332, USA. [8]Geology and Geophysics, Woods Hole Oceanographic Institution, Woods Hole, MA 02543, USA. [9]Oak Ridge National Laboratory, Oak Ridge, TN 37831–6016, USA. [10]Mathematics and Computer Science Division, Argonne National Laboratory, Argonne, IL 60439–4843, USA.

*To whom correspondence should be addressed. E-mail: zliu3@wisc.edu

end members for simulations under more realistic MWF.

The increase in MWF starting at 19 ka induces a gradual decrease in the AMOC (Fig. 1D). The associated freshwater anomaly is confined initially to the upper North Atlantic at H1 (fig. S1B) and is then transported in the upper ocean into the Southern Ocean, where it eventually spreads northward in the deep ocean, substantially freshening the glacial bottom water by the time of the BA (fig. S1C). From 17 ka to the BA, the MWF decreases in both experiments, leading to increases in the AMOC. The AMOC increases gradually toward the BA following the gradual decrease in MWF in DGL-B, but it

resumes abruptly at the BA following the abrupt termination of MWF in DGL-A (Fig. 1D). Regardless of the recovery speeds, however, the AMOC in both experiments peaks at ~19 sverdrup (1 sverdrup = 10^6 m^3/s) at the onset of the BA, or ~6 sverdrup greater than the glacial-state transport (~13 sverdrup), and is characterized by a deeper and stronger circulation (Fig. 2C), comparable with that in a Holocene simulation (not shown). The simulated transient responses of the AMOC from 19 to 14 ka, especially in experiment DGL-A, are in overall agreement with a reconstruction of changes in the AMOC export (Fig. 1D) (5).

Accompanying these changes in the AMOC is a bipolar seesaw response in surface temper-

ature until H1, followed by a global warming that peaks at the BA. The bipolar seesaw response is characterized by a cooling over the Northern Hemisphere and a warming over the Southern Hemisphere (Fig. 3A) and is caused by a decrease in the northward heat transport of the AMOC (28–30). The suppression of convection also contributes to the strong surface cooling in the North Atlantic. A weak warming also occurs over North America and northern Europe due to the lowering of the ice sheets and the associated response of the planetary waves (31). By contrast, the warming from H1 to BA is global, with the maximum warming relative to H1 exceeding 20°C in the North Atlantic and Arctic (Fig. 3B). A large fraction of this BA warming, or that part relative to the glacial state (Fig. 3C), is characterized by a polar amplification in both hemispheres.

The simulated global temperature evolution closely resembles paleoclimate reconstructions [supporting online material (SOM) Text 1], although there is a tendency for a model-data discrepancy before 19 ka, which may be attributed partly to our initial state of an equilibrium climate at LGM. Focusing on the Atlantic sector here, the simulated annual temperature closely follows the trajectory of temperature reconstructions from Greenland (Fig. 1E) and Antarctic (Fig. 1F) ice cores. From 21 to 19 ka, both Greenland and Antarctica show a weak early warming of ~0.5°C, which we attribute to increased obliquity and associated sea-ice feedback (32, 33). With the increased MWF from 19 to 17 ka, temperature decreases by 4°C over Greenland but increases by 2°C over Antarctica, reflecting the bipolar seesaw response (Fig. 3A). The most pronounced changes occur in response to the decrease in MWF from 17 to 14 ka. Simulated Greenland temperature increases by 15°C at the BA onset, comparable with temperature reconstructions (7, 34). By contrast, Antarctic temperature continues to increase toward the BA, as in ice-core reconstructions (35), which is caused primarily by the rapid increase in GHG concentrations during this period (SOM Text 2).

The characteristic North Atlantic temporal evolutionary structure of H1 cooling followed by BA warming simulated by CCSM3 is also in good agreement with sea-surface temperature (SST) reconstructions from the eastern subtropical gyre off the Iberian Margin (Fig. 1G). Over the tropical Atlantic, model SSTs first decrease toward H1 and then recover sharply at the BA, accompanied by a suppression of rainfall toward the H1 and a subsequent recovery toward the BA. The simulated rainfall suppression toward H1 (enhancement at BA) is caused by the southward (northward) migration of the Intertropical Convergence Zone (ITCZ), which is induced by the surface ocean warming south (north) of the equator in response to the increased (decreased) freshwater forcing (36). The simulated abrupt increase of SSTs and rainfall at the onset of the BA, especially in experiment DGL-A, generally

Fig. 1. Data-model comparison for several benchmark time series. (**A**) June insolation at 60°N (purple) (21) and atmospheric CO_2 concentration (green) (22). ppmv, parts per million by volume. (**B**) Sea level from the reconstruction (gray) (23) and model [meters of equivalent global sea level (ESL) for meltwater]. (**C**) Freshwater fluxes (FWF) in the model. (**D**) Pa/Th ratio at Bermuda (GGC5 core) as a proxy for AMOC export (5), and model maximum AMOC transport (below 500 m). (**E**) Greenland surface air temperature (SAT) based on Greenland Ice Sheet Project 2 (GISP2) δ^{18}O reconstruction with borehole temperature calibration (34) and in the model (model offset by −3°C). (**F**) Antarctic surface air temperature based on Dome C δ^{18}O reconstruction (35) and in the model. (**G**) SST from the Iberian Margin from reconstructions (8, 9) and model. (**H**) SST from the Cariaco Basin from reconstruction (10) and model (model offset by 4°C). (**I**) Rainfall in Cariaco Basin from reconstruction (11) and model. In (B) to (I), gray is used for the reconstruction, and red and blue for experiments DGL-A and DGL-B, respectively. The five circles on DGL-A in (D) represent the glacial state (GLA, 19 ka), H1 (17 ka), PreBA (14.7 ka), Recovery (REC, 14.5 ka), and BA (14.35 ka). All model variables are annual means with a 20-year running average. Overall, model simulations, especially DGL-A, are in good agreement with the proxy records, especially outside the tropical Atlantic. BP, before present.
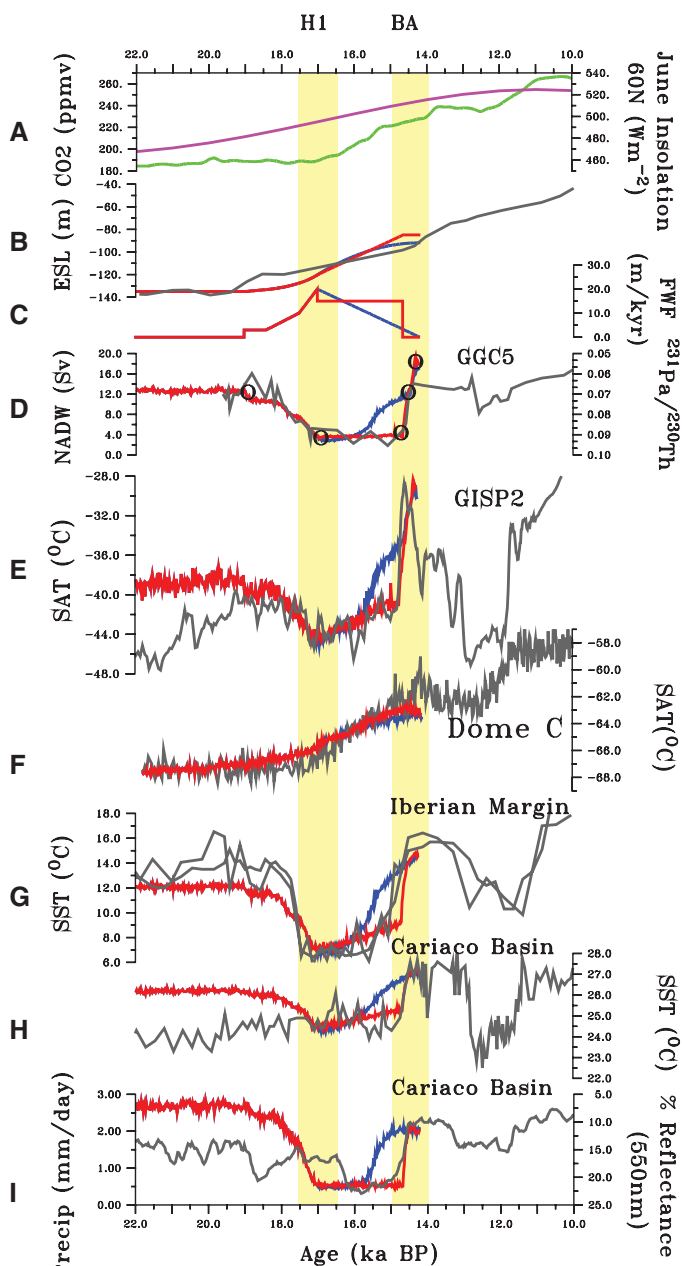
agree with the Cariaco Basin reconstructions (Fig. 1, H and I), although the simulated earlier decrease in the SST and rainfall toward H1 seems to be largely absent in the reconstructions. Overall, the model overestimates the climate variability associated with the ITCZ over the tropical Atlantic. This overestimation is likely caused by a double ITCZ bias in the model tropical Atlantic climatology—a common deficiency in most current CGCMs (37).

In contrast to the bipolar seesaw temperature response at the ocean surface, the subsurface ocean warms throughout the Atlantic during the MWF period from H1 to the BA (Fig. 2, E and F), providing a heat reservoir potentially important for the subsequent BA warming. The subsurface warming is largely consistent with previous experiments and observations (38). In the North Atlantic, the surface freshening suppresses the convective heat exchange, cooling the surface but warming the subsurface. The subsequent reduction of the AMOC and associated northward heat transport warms the entire South Atlantic water column, but further cools the surface North Atlantic.

Previous studies of the BA in simplified models found that the abrupt warming was caused by a sudden resumption of the AMOC in response to a gradual perturbation forcing, reflecting a strongly nonlinear response to MWF associated with substantial AMOC hysteresis (13–16). By contrast, CCSM3 simulates the BA warming largely as a linear response to MWF, with most of the abrupt warming occurring only in response to a sudden termination of the MWF. Indeed, CCSM3 has no appreciable hysteresis (SOM Text 3). This is best illustrated in experiment DGL-B from 19 to 14 ka (39, 40), whereby the AMOC decreases gradually from 19 to 17 ka when the MWF increases gradually, but then recovers gradually from 17 to 14.2 ka when the MWF decreases slowly, eventually overshooting beyond the glacial transport (Fig. 1, C and D) (41).

Both experiments DGL-A and DGL-B simulate a ~15°C warming over Greenland from H1 to BA, comparable with temperature reconstructions (7, 34) (Fig. 1). Of this amount, 5°C is associated with the AMOC recovery from H1 back to the glacial state, and the remaining 10°C results from the CO_2-induced warming and an AMOC overshoot (the AMOC recovery beyond the glacial-state transport). The approximate contributions of the three mechanisms can be assessed from experiment DGL-A. First, the total radiative warming due to CO_2 and orbital forcing in the absence of AMOC change can be estimated as the difference between the pre-BA (14.67 ka) and H1 states. In this period, the MWF and, in turn, the collapsed AMOC remain unchanged in DGL-A (Fig. 1, C and D), so that the warming is caused primarily by the radiative forcing. Indeed, from H1 to pre-BA, both Greenland and Antarctica exhibit a similar gradual warming of ~4°C (Fig. 1, E and F). This symmetric warming (fig. S6A) is consistent with the symmetric radiative forcing of CO_2 and annual

insolation. Our further sensitivity experiments show, however, that this warming is dominated by the CO_2 forcing, whereas the contribution of the orbital forcing is weak (SOM Text 2). Indeed, the period from 17 to 14.6 ka saw the first major rise of the GHGs, with a 40-ppm (parts per million) increase in CO_2 accounting for about half of the glacial-interglacial change (Fig. 1A). This large increase in CO_2 induces a symmetric global warming background for the subsequent BA warming.

Upon the suspension of the MWF after 14.67 ka in experiment DGL-A, the AMOC recovers rapidly to its glacial level by ~14.5 ka, with a 5°C warming over Greenland (Fig. 1, D and E). This recovery warming is of the same magnitude as the H1 cooling, reflecting a nearly linear dependence of Greenland temperature on AMOC strength. In contrast to the bipolar response to the MWF during H1 (Fig. 3A), however, the rapid warming due to AMOC recovery is confined to the North Atlantic and Arctic regions (Fig. 1, E to H, and fig. S6B).

Finally, after the recovery at 14.5 ka, Greenland temperature increases by another 6°C, peaking at 14.35 ka (Fig. 1E), accompanied by an AMOC overshoot beyond its glacial level by ~6 sverdrup (Fig. 1D). This BA overshoot, which generates a strong warming over the Nordic Sea region (Fig. 1, E to H, and fig. S6C), is caused by a natural overshoot of the AMOC at the end of MWF, which is further enhanced by the long duration of the MWF and the large CO_2 rise

from H1 to the BA. The overshoot appears to be caused by convective instability in the Nordic Sea on a background of deep-ocean warming (Fig. 2, E and F), as well as a basin-wide advective adjustment of salinity (SOM Text 4).

In contrast to the robust warming magnitude, the warming rate of the BA in CCSM3 depends critically on the MWF scenario. A faster reduction in MWF induces a more rapid BA warming, as seen by comparing experiments DGL-A and DGL-B. The sudden termination of MWF in DGL-A produces an abrupt BA warming that strongly resembles proxy records (Fig. 1), although the model warming is somewhat slower than in these records (300 versus 150 years, fig. S4). Because the natural adjustment time of the AMOC is ~300 years (as seen in experiment DGL-A), a similar abrupt BA warming can be induced in this model as long as there exists a substantial reduction of MWF several centuries before the Bølling onset. Because the two MWF scenarios DGL-A and DGL-B represent the end members, a more realistic MWF scenario that lies in between may also induce a rather rapid BA warming in CCSM3 (42). We conclude that the critical factor for producing the abruptness of the BA warming in CCSM3 is that the MWF to the North Atlantic keeps the AMOC near its off-state to within centuries of the Bølling onset, while other details of the meltwater history may not be essential.

We find that CCSM3 is able to simulate an abrupt BA warming as a transient response to a
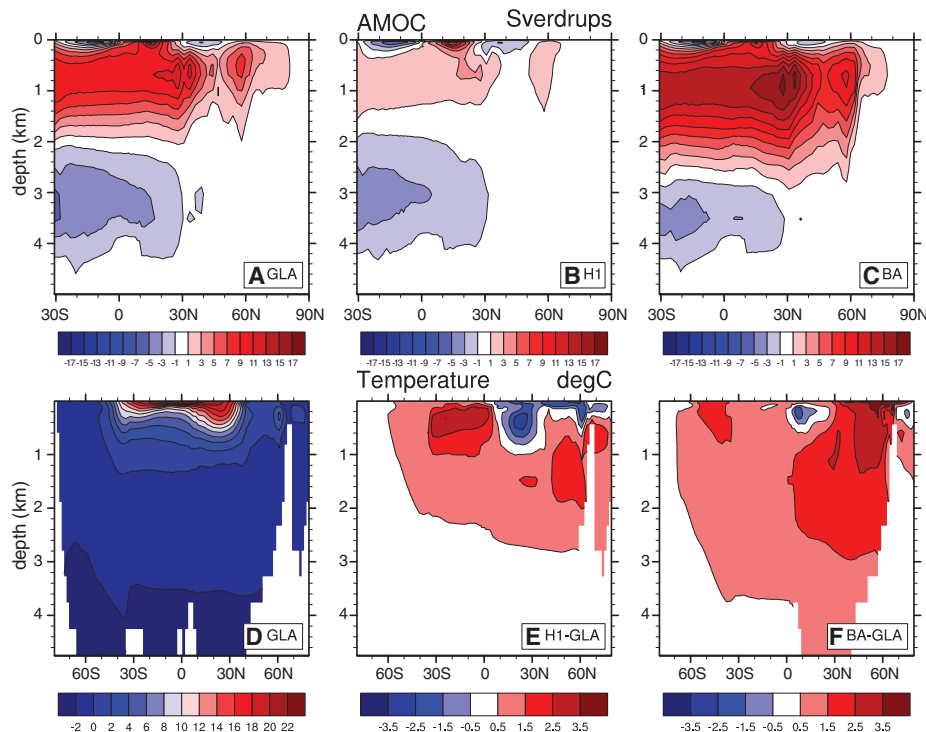

Fig. 2. AMOC streamfunction (in sverdrup) and Atlantic zonal mean temperature and temperature changes in experiment DGL-B (in °C). AMOC at (**A**) GLA, (**B**) H1, and (**C**) BA. Temperature at (**D**) GLA and temperature changes from the glacial state for (**E**) H1-GLA and (**F**) BA-GLA. The AMOC collapses in H1 and overshoots beyond the glacial state at BA. The subsurface ocean warms throughout the Atlantic, whereas the SST exhibits a bipolar seesaw response. (Each state is defined in Fig. 1D).

sudden termination of the North Atlantic MWF. The amplitude of the simulated BA is comparable to the amplitude reconstructed from paleoclimate proxies, notably in the North Atlantic and Antarctic regions. Our simulation suggests that the large BA warming is caused by the superposition of climate responses to increased atmospheric CO_2, the recovery of the AMOC from H1, and an AMOC overshoot. It remains uncertain if CCSM3 is successful in simulating the

abruptness of the BA warming inferred in proxy records. CCSM3 can produce the abruptness of the BA onset only if the MWF in the North Atlantic terminates within centuries before the BA. This is in contrast to previous work in simplified models, which exhibit a substantial AMOC hysteresis (39) such that an abrupt warming can be induced by a gradual change in MWF. The behavior of CCSM3, however, is typical of the current generation of CGCMs without flux

adjustment, which show little sign of substantial hysteresis (30, 43). Therefore, our results suggest that the current generation of CGCMs, like CCSM3, may not be able to induce an abrupt onset of BA warming under a gradual forcing. Is the current generation of CGCMs deficient in generating the abruptness of climate changes (44)? Is the AMOC hysteresis a fundamental feature of the real-world AMOC as suggested in intermediate models, or not essential as suggested in current CGCMs? Current observations are insufficient to address these questions unambiguously (SOM Text 5). We suggest that the critical observational evidence needed to clarify these fundamental issues is an accurate reconstruction of the rate of MWF before the BA.
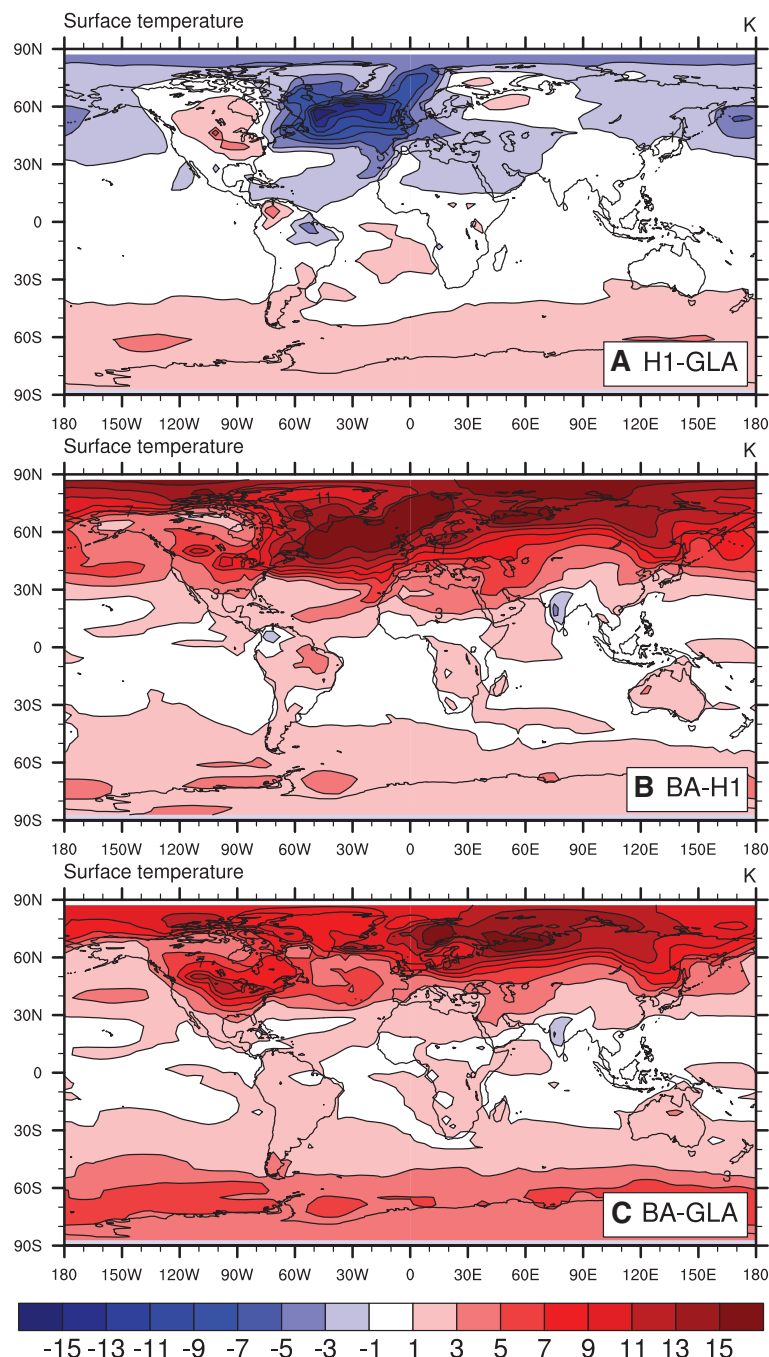

Fig. 3. Surface air temperature changes (in °C) in experiment DGL-B. (**A**) H1 temperature anomaly from the glacial state, (**B**) BA temperature anomaly from H1, and (**C**) BA temperature anomaly from GLA. The H1 temperature response exhibits a bipolar seesaw; the BA warming is dominated by a maximum warming at northern high latitude (B) over H1, but exhibits a more symmetric warming (C) over the glacial state. (Each state is defined in Fig. 1D.)

References and Notes
1. W. S. Broecker, *Paleoceanography* **13**, 119 (1998).
2. P. U. Clark, N. G. Pisias, T. F. Stocker, A. J. Weaver, *Nature* **415**, 863 (2002).
3. P. M. Grootes et al., *Nature* **366**, 552 (1993).
4. R. B. Alley, P. U. Clark, *Annu. Rev. Earth Planet. Sci.* **27**, 149 (1999).
5. J. F. McManus, R. Francois, J.-M. Gherardi, L. Keigwin, S. Brown-Leger, *Nature* **428**, 834 (2004).
6. E. Boyle, L. Keigwin, *Nature* **330**, 35 (1987).
7. J. P. Severinghaus, E. J. Brook, *Science* **286**, 930 (1999).
8. C. Waelbroeck et al., *Paleoceanography* **13**, 272 (1998).
9. E. Bard, F. Rostek, J.-L. Turon, S. Gandreau, *Science* **289**, 1321 (2000).
10. D. W. Lea, D. K. Pak, L. C. Peterson, K. A. Hughen, *Science* **301**, 1361 (2003).
11. L. C. Peterson, G. H. Haug, K. A. Hughen, U. Rohl, *Science* **290**, 1947 (2000).
12. In these simplified models, however, the transient simulations have not been carried out in a synchronously coupled mode under the complete climate forcing (notably the meltwater forcing), (45, 46).
13. A. Ganopolski, S. Rahmstorf, *Nature* **409**, 153 (2001).
14. G. Knorr, G. Lohmann, *Geochem. Geophys. Geosyst.* **8**, Q12006 (2007).
15. A. J. Weaver, O. A. Saenko, P. U. Clark, J. X. Mitrovica, *Science* **299**, 1709 (2003).
16. G. Knorr, G. Lohmann, *Nature* **424**, 532 (2003).
17. The nature of the AMOC resumption is complex from the perspective of a dynamic system (47) and is beyond the scope of this study.
18. S. Rahmstorf, *Nature* **378**, 145 (1995).
19. S. G. Yeager, C. A. Shields, W. G. Large, J. J. Hack, *J. Clim.* **19**, 2545 (2006).
20. B. L. Otto-Bliesner et al., *J. Clim.* **19**, 2526 (2006).
21. A. Berger, *J. Atmos. Sci.* **35**, 2362 (1978).
22. F. Joos, R. Spahni, *Proc. Natl. Acad. Sci. U.S.A.* **105**, 1425 (2008).
23. W. R. Peltier, *Annu. Rev. Earth Planet. Sci.* **32**, 111 (2004).
24. For technical reasons, river run-off routing is kept as at the present.
25. B. L. Otto-Bliesner et al., *Geophys. Res. Lett.* **34**, L12706 (2007).
26. J. Lynch-Stieglitz et al., *Science* **316**, 66 (2007).
27. P. U. Clark, A. C. Mix, *Quat. Sci. Rev.* **21**, 1 (2002).
28. T. Crowley, *Paleoceanography* **7**, 489 (1992).
29. T. F. Stocker, *Science* **282**, 61 (1998).
30. R. Stouffer et al., *J. Clim.* **19**, 1365 (2006).
31. S. W. Hostetler, P. U. Clark, P. J. Bartlein, A. C. Mix, N. G. Pisias, *J. Geophys. Res.* **104**, 3947 (1999).
32. S.-I. Shin, Z. Liu, B. Otto-Bliesner, J. Kutzbach, S. J. Vavrus, *Geophys. Res. Lett.* **30**, 1096 (2003).
33. A. Timmermann, O. Timm, L. Stott, L. Menviel, *J. Clim.* **22**, 1626 (2009).
34. K. Cuffey, G. Clow, *J. Geophys. Res.* **102**, 26383 (1997).
35. J. Jouzel et al., *Science* **317**, 793 (2007).
36. R. Zhang, T. Delworth, *J. Clim.* **18**, 1853 (2005).
37. M. K. Davey et al., *Clim. Dyn.* **18**, 403 (2002).

38. This subsurface warming is qualitatively similar to that of previous experiments with North Atlantic MWF, especially in the tropical region and Southern Hemisphere [e.g., (30, 48)]; it seems also to be consistent with benthic $\delta^{18}O$ inferred temperature changes in the tropical Atlantic (49), western subtropical North Atlantic (4), and Nordic Sea (50), as well as Mg/Ca-based benthic temperatures from the eastern subtropical North Atlantic (51).

39. S. Rahmstorf et al., Geophys. Res. Lett. 32, L23605 (2005).

40. The MWF varies slowly during this period at a rate of ~0.1 sverdrup/ky in DGL-B, comparable to that used in previous standard hysteresis tests (18, 39).

41. About a third of the model BA warming appears to be associated with a nonlinear convective response in the Nordic Sea. As seen in experiment DGL-B, under a gradual forcing, the AMOC and Greenland temperature, after a long period of gradual change, increase abruptly at the end stage (14.6 ka) in 100 years (6 sverdrup and 6°C), nearly identical to the last 100 years of warming in experiment DGL-A (Fig. 1, D and E, and fig. S4). This abrupt warming is induced by regional convective instability in the Nordic Sea (18) on a background deep-ocean warming (52) and is enhanced by the northward heat transport associated with the enhanced AMOC.

42. With a slower reduction in MWF, the AMOC resumption and attendant BA warming in CCSM3 usually occur faster than the rate at which the MWF is reduced, partly due to

the convective instability process in the Nordic Sea (41). In a deglaciation sensitivity experiment similar to DGL-B, but with a faster termination time of 2000 years, the BA warming takes only 500 years, substantially faster than the MWF itself (not shown).

43. Except for an earlier generation of CGCM with flux adjustments (53, 54), all published results from CGCMs are similar to those of CCSM3 in showing that the AMOC recovers its strength after the termination of the freshwater pulse. Because these CGCM hosing experiments are usually short (<1000 years), they are not strict tests for the hysteresis of AMOC (18). Nevertheless, these models have shown little sign of substantial hysteresis.

44. A diagnosis of nine coupled climate models, including both CGCMs and intermediate models, suggests a positive bias in the freshwater transport by the AMOC in the South Atlantic, which may imply a bias toward a more stable AMOC and therefore a lack of multiple equilibria and in turn substantial hysteresis in these climate models (55). Further study is needed, however, to understand the stability of the AMOC in coupled climate models, especially in state-of-art CGCMs.

45. D. J. Lunt, M. S. Williamson, P. J. Valdes, T. M. Lenton, Clim. Past Discuss. 2, 267 (2006).

46. O. Timm, A. Timmermann, J. Clim. 20, 4377 (2007).

47. J. Abshagen, A. Timmermann, J. Phys. Oceanogr. 34, 2756 (2004).

48. S. Manabe, R. Stouffer, Paleoceanography 12, 321 (1997).

49. C. Ruhlemann et al., Paleoceanography 19, PA1025 (2004).

50. T. L. Rasmussen, E. Thomsen, Palaeogeogr. Palaeoclimatol. Palaeoecol. 210, 101 (2004).

51. L. Skinner, N. Shackleton, Quat. Sci. Rev. 25, 3312 (2006).

52. J. Mignot, A. Ganopolski, A. Levermann, J. Clim. 20, 4884 (2007).

53. S. Manabe, R. Stouffer, J. Clim. 1, 841 (1988).

54. J. Yin, R. Stouffer, J. Clim. 20, 4293 (2007).

55. S. Weber et al., Clim. Past Discuss. 3, 51 (2007).

56. We thank A. Ganoposki, J. Marotzke, and A. Timmermann for helpful discussions and two reviewers for comments. This research was supported mainly by the Paleoclimate Program of NSF, NCAR, and Chinese NSF (NSFC40875058). The computing is supported by the U.S. Department of Energy INCITE program and Abrupt Climate Change Program. This paper is CCR contribution No. 980.

Undulatory Swimming in Sand: Subsurface Locomotion of the Sandfish Lizard

Ryan D. Maladen,[1] Yang Ding,[2] Chen Li,[2] Daniel I. Goldman[1,2]*

The desert-dwelling sandfish (*Scincus scincus*) moves within dry sand, a material that displays solid and fluidlike behavior. High-speed x-ray imaging shows that below the surface, the lizard no longer uses limbs for propulsion but generates thrust to overcome drag by propagating an undulatory traveling wave down the body. Although viscous hydrodynamics can predict swimming speed in fluids such as water, an equivalent theory for granular drag is not available. To predict sandfish swimming speed, we developed an empirical model by measuring granular drag force on a small cylinder oriented at different angles relative to the displacement direction and summing these forces over the animal movement profile. The agreement between model and experiment implies that the noninertial swimming occurs in a frictional fluid.

The locomotion of organisms (1, 2), whether by running, flying, swimming, or crawling, is the result of multiple-degree-of-freedom nervous and musculoskeletal systems interacting with an environment that often flows and deforms in response to movement. Nearly all experiments and models of terrestrial locomotion have been developed for running and walking on rigid, flat, no-slip frictional substrates for which the complication of substrate flow is not considered. In contrast, complexity in interaction with the environment in aquatic and aerial locomotion (swimming and flying) is well recognized (3). Determining mechanisms for propulsion or lift in these media is

always possible in principle because the rules of interaction with fluids are worked out: They require solving Navier-Stokes hydrodynamics in the presence of moving boundary conditions. A major challenge in biology is to understand the locomotion of organisms that walk, crawl, or burrow on or within terrestrial substrates like sand (4), soil (5), and muddy sediments (6) that display both solid and fluidlike behavior. In such materials, validated theories such as the Navier-Stokes equations for fluids do not exist, and visualization techniques [such as particle image velocimetry in fluids (7)] are nearly nonexistent. Understanding of the mechanics of subsurface movement has ecological importance and could reveal how the actions of small burrowing organisms can transform entire landscapes (8).

Animal burrowing and movement within granular media is relevant to desert organisms like scorpions, snakes, and lizards that move within sand to escape heat and predators and hunt

for prey (9, 10). Desert sand [which covers 6 to 10% of land surface (11)] is an example of a granular material, a collection of dissipative particles that interact through contact forces and in bulk can display solid and fluidlike features (12) when disturbed. A key parameter that controls the response of granular media to intrusion is the volume fraction ϕ, the ratio of material volume to total occupied volume. In dry granular media in natural environments, ϕ depends on the history of the sand (for example, perturbations by wind or animal burying and digging), and can vary between 0.57 and 0.64 (13). The response of granular media to intrusion depends on ϕ: Closely packed material at high ϕ must expand to flow, whereas loosely packed material at low ϕ consolidates (14). The effects of ϕ on drag are largely unexplored, although we have recently found that vertical penetration resistance doubles as ϕ increases by just 0.08 (15).

To investigate how rheological features of the material influence the locomotor mode and performance of an organism moving within sand, we used high-speed x-ray imaging to study a small (~10 cm) desert-dwelling lizard, the sandfish, that inhabits the Saharan desert of Africa and moves within granular media of different ϕ. The sandfish's above-ground burial process has been described (9), and it is hypothesized that its counter-sunk lower jaw and smooth scales with low friction and low wear properties (16) aid swimming and digging. However, little is known about how the animal moves subsurface. Although it has been hypothesized that body motion plays an important role in thrust production (9, 17) in sand-dwelling lizards, a recent study using nuclear magnetic resonance (NMR) to visualize subsurface motion proposed that the sandfish used its limbs in a paddling motion along with undulations on its body to generate thrust subsurface (18). However, the observa-

[1]Interdisciplinary Bioengineering Program, Georgia Institute of Technology, Atlanta, GA 30332, USA. [2]School of Physics, Georgia Institute of Technology, Atlanta, GA 30332, USA.

*To whom correspondence should be addressed. E-mail: daniel.goldman@physics.gatech.edu

Supporting Online Material for

Transient Simulation of Last Deglaciation with a New Mechanism for Bølling-Allerød Warming

Z. Liu, [*] B. L. Otto-Bliesner, F. He, E. C. Brady, R. Tomas, P. U. Clark, A. E. Carlson, J. Lynch-Stieglitz, W. Curry, E. Brook, D. Erickson, R. Jacob, J. Kutzbach, J. Cheng

*To whom correspondence should be addressed. E-mail: zliu3@wisc.edu

This PDF file includes:

> Materials and Methods
> SOM Text
> Figs. S1 to S7
> References and Notes

Other Supporting Online Material for this manuscript includes the following:
(available at www.sciencemag.org/cgi/content/full/325/5938/310/DC1)

> Movie S1

SOM, BA_Science, Liu et al., revision2, 05/07/2009

Materials and Method

1: Model Setup: The CGCM employed is the National Center for Atmospheric Research (NCAR) CCSM3 with a dynamic global vegetation module. CCSM3 is a global, coupled ocean–atmosphere–sea ice–land surface climate model without flux adjustment (*S1*). All the simulations were performed in the version of T31_gx3v5 resolution (*S2*). The atmospheric model is the Community Atmospheric Model 3 (CAM3) with 26 hybrid coordinate levels in the vertical and ~3.75-degree resolution in the horizontal. The land model uses the same resolution as the atmosphere, and each grid box includes a hierarchy of land units, soil columns, and plant types. Glaciers, lakes, wetlands, urban areas, and vegetated regions can be specified in the land units. The ocean model is the NCAR implementation of the Parallel Ocean Program (POP) in vertical *z*-coordinate with 25 levels. The longitudinal resolution is 3.6-degree and the latitudinal resolution is variable, with finer resolution near the equator (~0.9 degrees). The sea ice model is the NCAR Community Sea Ice Model (CSIM). CSIM is a dynamic-thermodynamic model that includes a subgrid-scale ice thickness distribution. The resolution of CSIM is identical to that of POP. The preindustrial control simulation reproduces the major features of global climate, notably in the deep ocean (*S3*).

The Last Glacial Maximum (LGM) CCSM3 simulation has a global cooling of 4.5°C compared to pre-industrial with amplification of this cooling at high latitudes and over the continental ice sheets (*S3*). The LGM control run also simulates a shoaling of North Atlantic Deep Water and farther northward penetration of Antarctic Bottom Water (*S4*). A 1,800-year LGM equilibrium simulation was branched off from an earlier LGM simulation in order to incorporate the dynamic global vegetation model and to reduce the

model drift in the deep ocean. The transient simulation was then started at the end of the 1,800-year LGM/DGVM equilibrium run with the transient orbital parameter starting at 22 ka. The transient concentrations of the greenhouse gases (CO_2, CH_4 and N_2O) were adopted from ref S5. The continental ice sheets were modified approximately once per thousand year according to the ICE-5G reconstruction (*S6*). The coastlines at LGM were also taken from the ICE-5G reconstruction and were not modified during the simulations in this study.

2: Meltwater Scheme: Since the meltwater flux (MWF) from the retreat of the ice sheets is not well constrained during the last deglaciation, we adopted simple schemes of MWF (Fig.1c) and considered only two regions to impose MWF: one in the North Atlantic region between 50°N and 70°N, and the other in the Gulf of Mexico. From 19 ka to 18.4 ka, the first pulse of MWF was imposed at the rate of 3 m/kyr (1m/kyr = 0.0115 Sv; 1 m/kyr refers to 1 meter of equivalent global sea level rise per thousand year) over the North Atlantic. From 18.4 ka to 17.5 ka, the MWF was linearly increased from 0 to 5 m/kyr in the Gulf of Mexico and from 3 to 5 m/kyr in the North Atlantic. From 17.5 ka to 17.0 ka, the MWF remained at 5 m/kyr in the Gulf of Mexico and linearly increased from 5 to 15 m/kyr in the North Atlantic. Starting from 17 ka, two schemes of MWF were employed to test the sensitivity of the climate system to the rate of the MWF termination. In scheme DGL-B (Fig.1c, blue), the MWF linearly decreased from 20 to 0 m/kyr from 17 ka to 14.2 ka. In scheme DGL-A (Fig.1c, red), the MWF in the Gulf of Mexico was shut off immediately after 17.0 ka, while the MWF in the North Atlantic remained at 15 m/kyr until 14.67 ka when it was abruptly shut off.

Supporting online text

1: Global Temperature Response during Deglaciation: The MWF in the North Atlantic forces significant remote climate responses throughout the globe via climatic teleconnections (*S7*). Overall, Northern Hemisphere surface temperature evolves similarly to Greenland (Figs.1g-i), but Southern Hemisphere temperature increases monotonically as over the Antarctic. The overall global surface temperature evolution can be seen clearly in the two leading EOFs during the deglaciation (Fig.S3), which are in excellent agreement with the corresponding EOFs derived from surface temperature proxy records from the last deglaciation (*S8*). The first EOF mode exhibits an overall global warming that tends to increase monotonically as in the Antarctica (Fig.S3a); this mode is caused predominantly by the rising CO_2 and orbital forcing (Fig.1a). In contrast, the second EOF mode exhibits a bipolar seesaw response that evolves similarly to the Greenland temperature (Fig.S3b); this mode is associated with the North Atlantic MWF (Fig.1c) through climate teleconnections.

2. GHG vs Orbital Forcing on BA Warming: To assess the contributions of CO_2 and orbital forcing to BA warming, we performed two sensitivity experiments from H1 to BA that are forced the same as Exp. DGL-A (but with the AMOC effect excluded) except with the transient GHG forcing (CO_2 experiment) and orbital forcing (orbital experiment) imposed separately, keeping all remaining factors at the H1 (17 ka) value. Fig.S4 shows the temperature evolution over Greenland and Antarctic for Exp. DGL-A (black), CO_2 experiment (green solid) and orbital experiment (green dash) from H1 to BA. It is seen

that the warming in DGL-A is largely contributed by the CO_2 experiment. A further calculation shows that the zonal mean surface warming at high latitudes ($>60^o$) is 3 times greater in the CO_2 experiment than in the orbital experiment (~3^oC vs ~1^oC). The CO_2 forcing is even more dominant in the tropics ($<30^o$ latitude), with a surface warming of ~1^oC in the CO_2 experiment, but almost zero or slight cooling in the orbital experiment, the slight cooling in the latter being induced by the reduction of annual insolation associated with the increase of obliquity. For the global average, the surface warming is 6 times larger in the CO_2 experiment than in the orbital experiment (1.51^oC vs 0.25^oC). From these experiments, we conclude that the warming in Exp. DGL-A from H1 to pre-BA is dominated by the CO_2 forcing.

3. AMOC Hysteresis in CCSM3: The lack of a significant hysteresis in CCSM3 is seen more clearly in the "hysteresis diagram," in which the model AMOC transport is plotted against the MWF (Fig.S5). As the MWF increases, the AMOC diminishes almost linearly, in contrast to many theoretical and intermediate climate models (*S9-S11*). In addition, as the MWF decreases, the model AMOC largely follows a trajectory of gradual recovery, instead of staying in the off-mode. Furthermore, we have performed dozens of hosing sensitivity experiments similar to those in other models, with the MWF over various regions and of various lengths, in both glacial state and Holocene state (not shown). Our experiments, and similar hosing experiments that have been carried out previously in CCSM3 (e.g. *S12*), all show a recovery of the AMOC as soon as the MWF stops. We have found no evidence of a significant hysteresis and multiple equilibria in CCSM3.

4: Mechanisms for the AMOC Overshoot: At the end of a freshwater pulse, the model AMOC tends to exhibit an overshoot beyond its pre-hosing level, inducing strong warming in the high latitude North Atlantic that lasts a few centuries after the freshwater termination. For the BA warming, this overshoot is associated partly with the strong subsurface warming in response to the long MWF during H1 (Fig.2f), which when the MWF is terminated, destabilizes the convection in the Nordic Sea (*S13*) and heats the atmosphere through an increased upward surface heat flux. The strong CO_2 warming is also important for the melting of sea ice in the Nordic Sea, and in turn the sudden onset of deep convection in this region.

Another possible mechanism for the overshoot is a basin-wide salinity adjustment. This can be demonstrated in a 3-box model that consists of a single polar box that combines the surface and deep polar boxes together for representing the region of deep convection (*S14*) (Fig.S7a) (or a 4-box model with the surface and deep polar boxes separated (*S15*)). In its simplest form, the temperatures are fixed in each box while the salinity is forced by a freshwater flux forcing. This type of box model fundamentally differs from the classical Stommel box model (*S16*) in the inclusion of a deep polar water box that is separated from a deep tropical water box. Damped oscillatory eigenmodes are generated, which lead to a slow overshoot of the AMOC in response to a meltwater pulse as shown in the example in Fig.S7a. In response to a MWF between years 1-300, salinity and the attendant density decrease rapidly in the polar box, reducing the southward pressure gradient at depth and, therefore, the AMOC transport. With the termination of the meltwater flux at year 300, the salinity increases rapidly in the polar box because of

the fast recovery in the deep convection region. The recovery of the deep tropical salinity, however, lags behind the polar box. As a result, the polar box becomes saltier than the deep tropical box at year 360, generating an equatorward pressure gradient anomaly (relative to pre-hosing) in the deep ocean, which eventually leads to an overshoot of the AMOC beyond its pre-hosing level at year 430, with the peak at year 530. In the mean time, the surface tropical box becomes fresher because of the increased freshwater transport from below. This also contributes to an anomalous equatorward pressure gradient at depth, enhancing the overshoot. The key factor for this overshoot is the slower response time of the deep tropical ocean than the polar region, which creates a delay of the deep tropical salinity, and in turn an anomalous deep pressure gradient that is needed for the AMOC overshoot.

This slow tropical deep ocean recovery for the overshoot appears to be operating in CCSM3 at glacial times, as illustrated in an idealized hosing experiment. For CCSM3, the three ocean boxes are averaged as: surface tropical box (box 1, 45^oS – 20^oS, 0 - 500-m), polar box (box 2, 35^oN – 80^oN, 0 – 2000-m) and deep tropical box (box 3, 45^oS – 20^oS, 500 – 2000-m). The evolution of the AMOC transport and the salinities of the three boxes are plotted for CCSM3 (Fig.S7b) similarly as for the box model (Fig.S7a). The CCSM3 shares a key feature of the overshoot with the box model: the earlier recovery of the polar ocean salinity than the deep tropical salinity. This AMOC overshoot is accompanied by a modest overshoot warming in the Nordic Sea region (3^oC over Greenland), but little signal to the south (not shown). In the transient simulations with complete forcing in DGL-A and B, the overshoot is likely to be contributed by both the convection mechanism and the salinity adjustment mechanism.

SOM, BA_Science, Liu et al., revision2, 05/07/2009

It remains unclear if the short (centennial) AMOC overshoot in CCSM3 existed in observation. The proxy for AMOC export (Pa/Th ratio in at Bermuda, Fig.1d, S17) does not exhibit an overshoot signal. This lack of overshoot signal, however, could be due to the poor temporal resolution or the long mixing time scale of the proxy itself. In addition, this lack of overshoot may be due to the location of this proxy. Dynamically, the short overshoot event is likely to be recorded more clearly along the deep western boundary current than in the interior ocean, because the deep western boundary current is affected by the upstream perturbation rapidly through the boundary current advection and boundary waves, while the interior ocean is affected by slow adjustment of interior advection and radiating Rossby waves from the eastern boundary. The proxy for AMOC export is located in the interior ocean on the Bermuda Rise (*S17*) and therefore may not be able to record the overshoot signal. In contrast, a recent high resolution proxy for deep western boundary current speed from the Eirik Drift shows a clear short overshoot at Bølling warming (*S18*). This location dependence of the overshoot signal is indeed consistent with our model, which shows no overshoot signal in the bottom water near Bermuda, but shows a clear overshoot signal at the Eirik Drift (not shown). Therefore, more high resolution data along the western boundary are needed to assess the existence of an overshoot signal.

5: Is CCSM3 Consistent with Observations for the Abrupt BA Warming? To our knowledge, CCSM3 is consistent with the observed abrupt BA warming within the observational uncertainty, largely because the precise history of MWF prior to BA remains highly uncertain. Indeed, MWF is the derivative of, and therefore much more

uncertain than, the sea level history. Furthermore, the global sea level change, which accounts for the accumulated MWF of all the sources, has a significant uncertainty in both the timing and magnitude (*S19-S21*). The CCSM3 scenarios for MWF are consistent with some reconstructions, considering the uncertainties. For example, the meltwater during H1 has been suggested to have occurred, in certain regions, in two pulses, H1A and H1B (*S22*). The later pulse H1A occurred between 16 ka and just before BA and may represent the last meltwater pulse whose termination could cause the abrupt BA. In addition, Clark et al. (*S23*) suggest that H1 MWF was bracketed by two major rerouting events into the Hudson River (R8 and R7). The later event (R7) is ~1000 kyr in duration and terminated just before BA. They argued that the combination of R8, H1, and R7 was responsible for the cold period prior to the Bølling, and the final rerouting that terminated R7 was a trigger for the BA warming. Alternatively, the abrupt BA may be caused by a slow stochastic meltwater forcing, via the so called stable collapse in a mono-stable system, as occurred in some climate-ecosystem models (*S24*).

Finally, MWP-1A (*S25, S26*) can also be accommodated in CCSM3. Weaver et al. (*S27*) proposed that the BA was triggered by MWP-1A as a MWF from the Antarctic Ice Sheet, switching the AMOC equilibrium from the off-mode to the on-mode. In CCSM3, however, an Antarctic MWF the same as in ref. S27 fails to generate a BA warming (not shown). Instead, the MWF weakens the AMOC slightly through the upper ocean transport of freshwater into the North Atlantic, as in other GCMs (*S28*). Nevertheless, MWP-1A can be accommodated as a meltwater discharge from the Antarctic Ice Sheet (*S29*) contemporaneous with (*S30, S31*), instead of preceeding (*S18*), the BA, which is possible within dating uncertainties. As such, a large amount of

meltwater of MWP-1A is "hidden" in the Southern Ocean without a significant global impact. The other possibility is that a significant outflow of MWP-1A entered the Gulf of Mexico as hyperpycnal flow (*S32*). However, in current model simulations the hyperpycnal flow still is transported eventually into the North Atlantic, where it weakens the AMOC (*S33*), and recent analyses of runoff records suggests that <13% of the total MWP-1A volume entered the Gulf of Mexico as either a hyperpycnal or hypopycnal flow (*S34*).
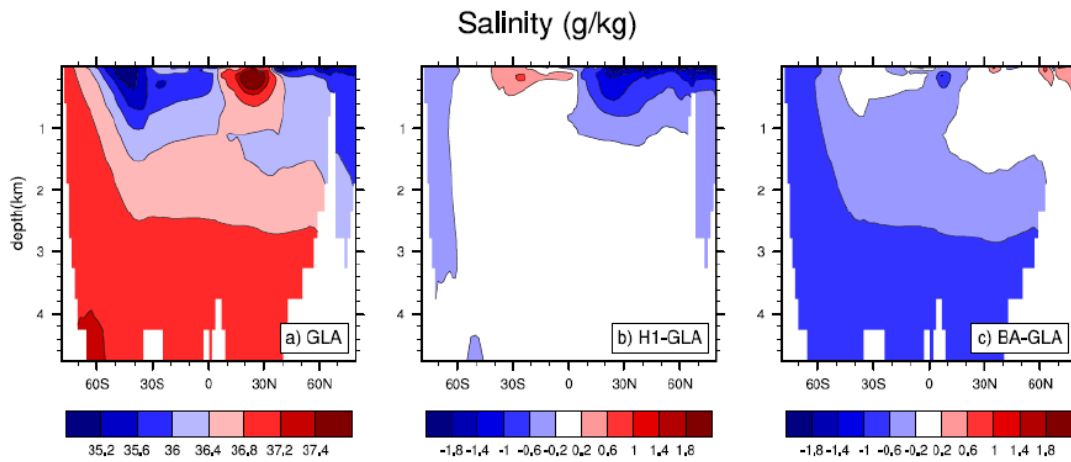
Fig.S1:Atlantic basin zonal mean salinity in exp. DGL-B. for (a) GLA state, (b) H1-GLA, (c) BA-GLA.. It shows the transport of freshwater anomaly from the surface North Atlantic in (b) to the deep ocean through the Antarctic Bottom Water in (c). The continuous evolution of the zonal mean salinity can be seen in the supporting movie 1.
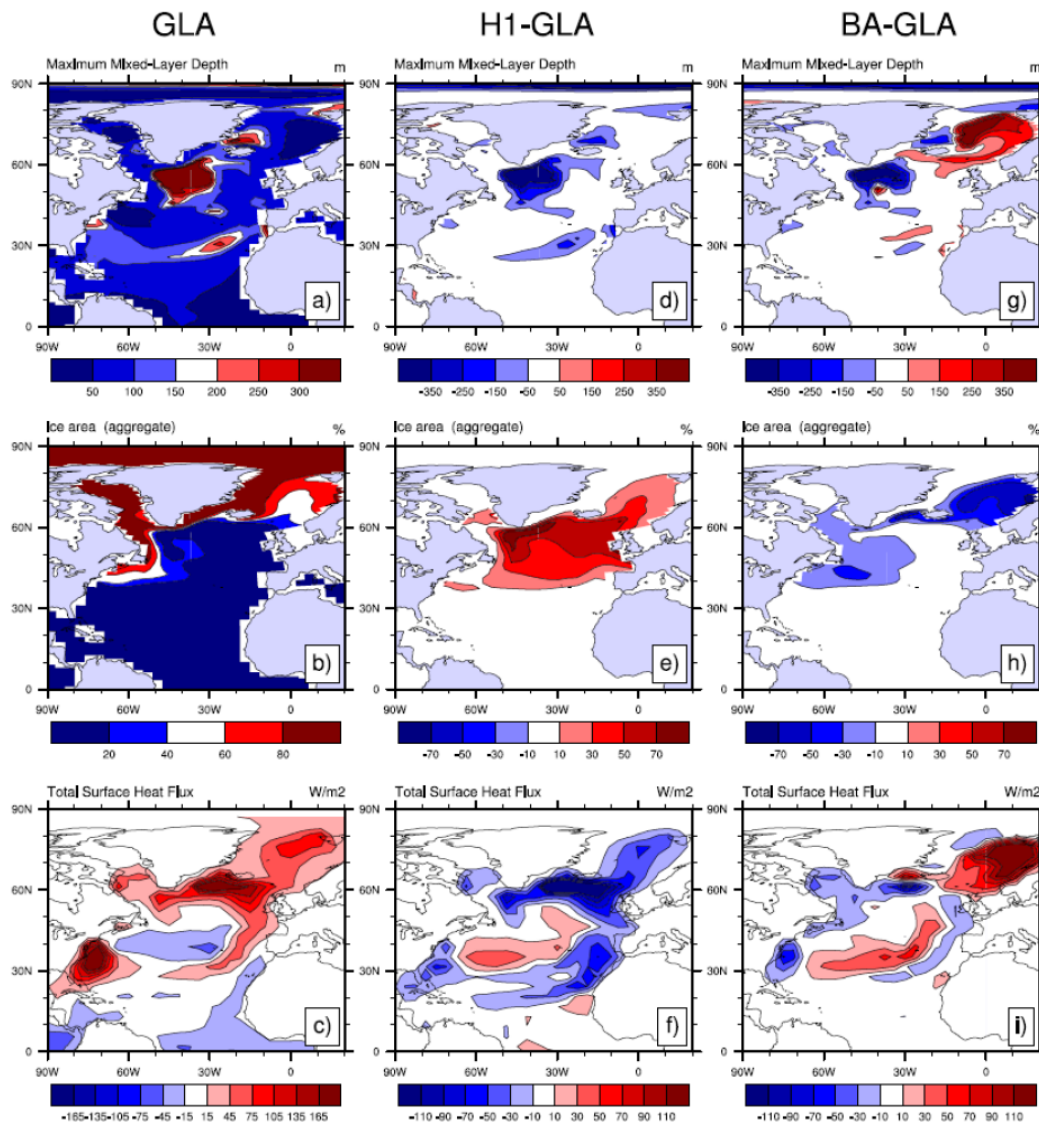
Fig.S2: Model North Atlantic maximum mixed layer depth, (m), sea ice area coverage (%), and surface heat flux (w/m², positive upward) for (a-c) LGM , (d-f) H1-LGM and (g-i) BA-LGM. It is shown that deep convection in Labrador Sea at GLA is shut off at H1 , with a sea ice expansion and loss of heat flux to the atmosphere. Deep convection is then resumed in the East Greenland Sea at BA, with the retreat of sea ice and a significant release of heat flux into the atmosphere, similar to a Holocene simulation (not shown).
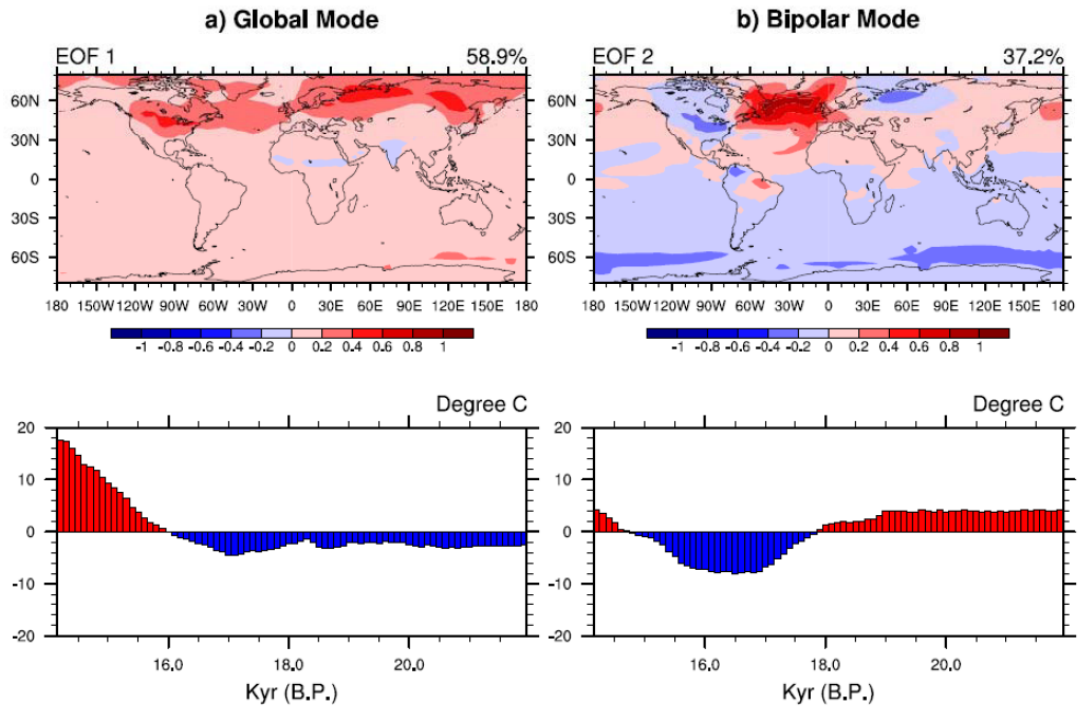
Fig.S3) (a) EOF1 and (b) EOF2 (upper pattern, lower time series) of global surface air temperature in Exp. DGL-B. The EOF1 exhibits a global warming with the evolution similar to Antarctic temperature, while EOF2 exhibits a bipolar seesaw with the evolution similar to Greenland temperature. These two EOFs are in good agreement with the EOFs of the SST reconstruction of ref. S8.. (EOF is normalized, while the time series has the unit of $^{\circ}C$).
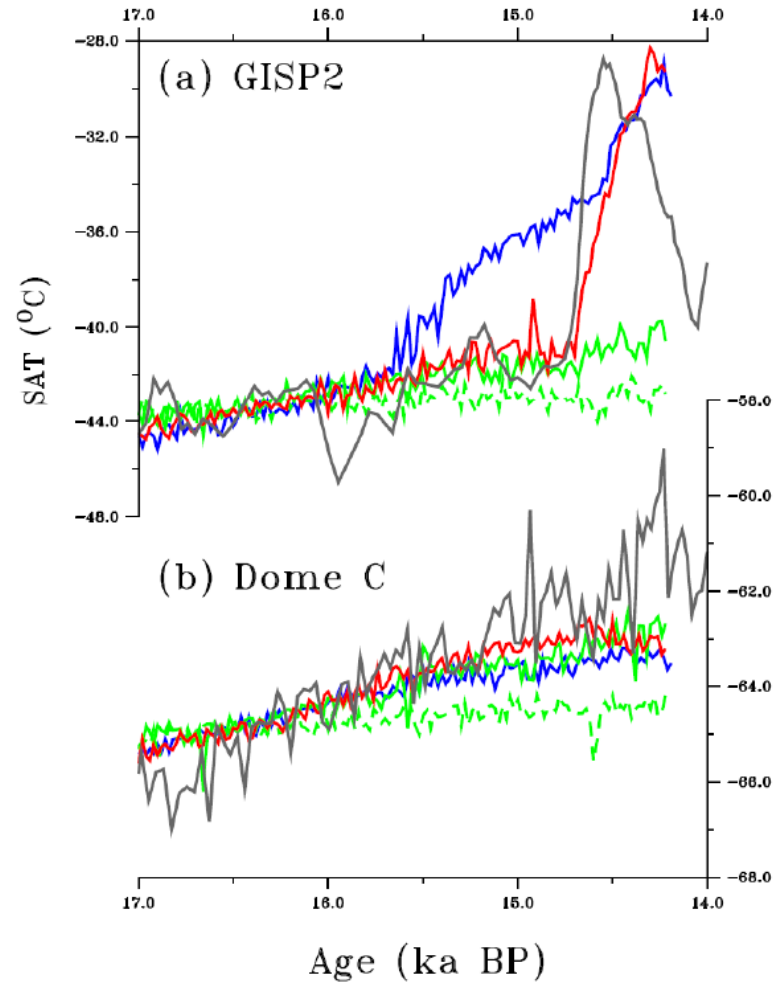
Fig.S4: Temperature (20-year running mean) evolution at (a) Greenland and (b) Dome C from H1 to BA for two sensitivity experiments that are forced the same as in Exp. DGL-A except that the transient CO_2 (CO_2 experiment, solid green) and insolation (orbital experiment, dash green) forcing is imposed separately starting at 17 ka. For comparison, the corresponding temperature evolution in the observation (black), Exp. DGL-A (red), DGL-B (blue) are also plotted the same as in Fig.1. It is clear that the warming in DGL-A is caused predominantly by the increase of CO_2.
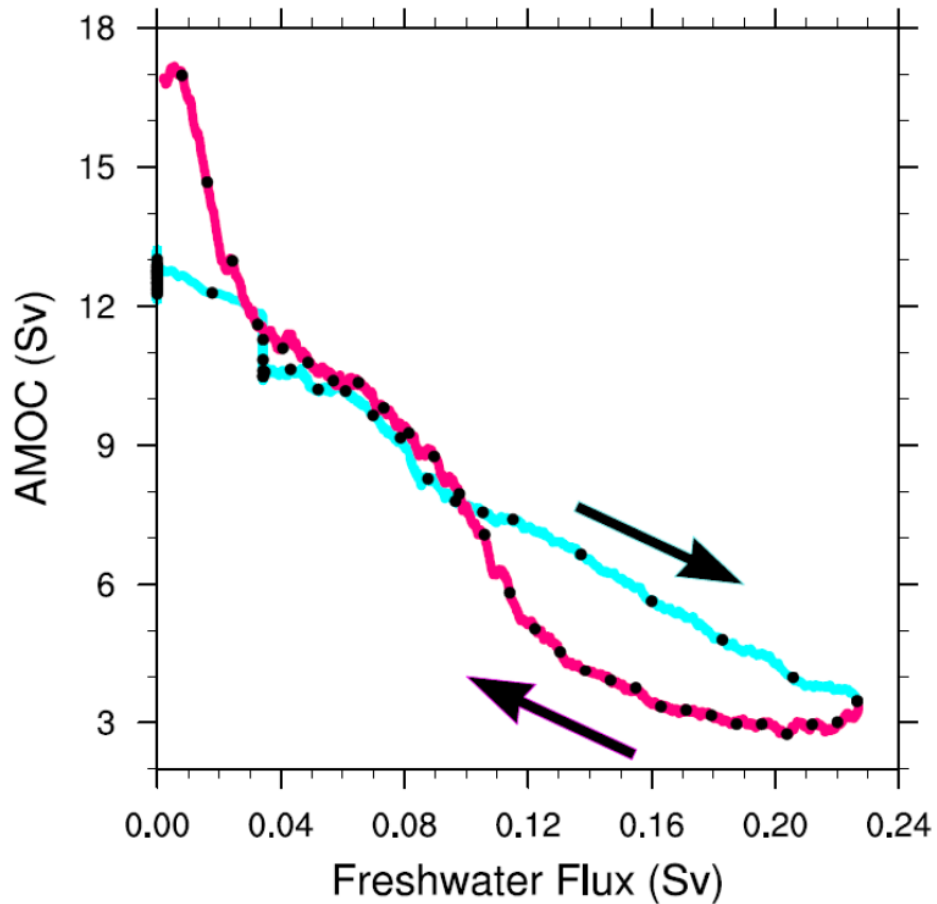
Fig.S5: "Hysteresis diagram" showing the AMOC transport (maximum transport below 500-m) (after a 50-year running mean) as a function of the prescribed meltwater flux in Exp. DGL-B. (Each dot for a 100-yr mean. Blue for the early part and purple for the later part). The AMOC shows no significant hysteresis: when the freshwater flux is increased, the AMOC diminishes almost linearly; when the freshwater flux is reduced, the AMOC transport can barely stay at the constant level of a AMOC-off state.
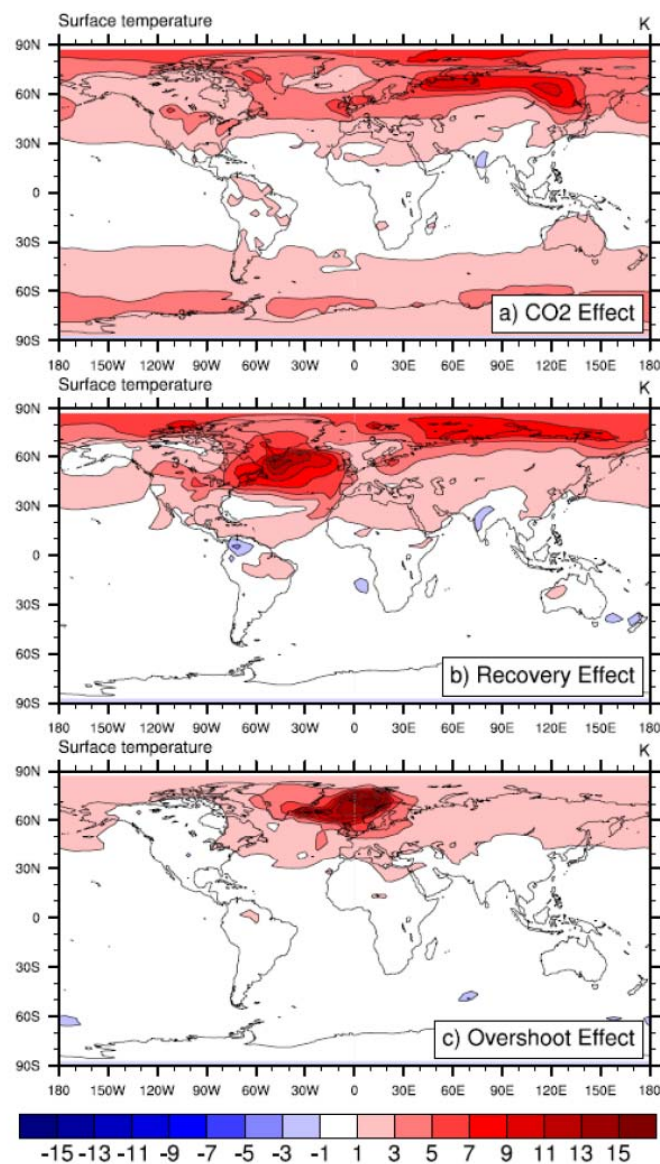
Fig.S6: Three components of the total BA warming above H1 in surface air temperature (°C) (BA-H1 in Fig.3b) as estimated in Exp. DGL-A. (a) Radiative effect due to CO_2 (PreBA-H1), (b) Recovery Effect (REC- PreBA), (c) Overshoot effect (BA-REC). (each state is defined in Fig.1d). The CO_2 effect is predominantly hemispherically symmetric, while the other two are confined in the North Atlantic.
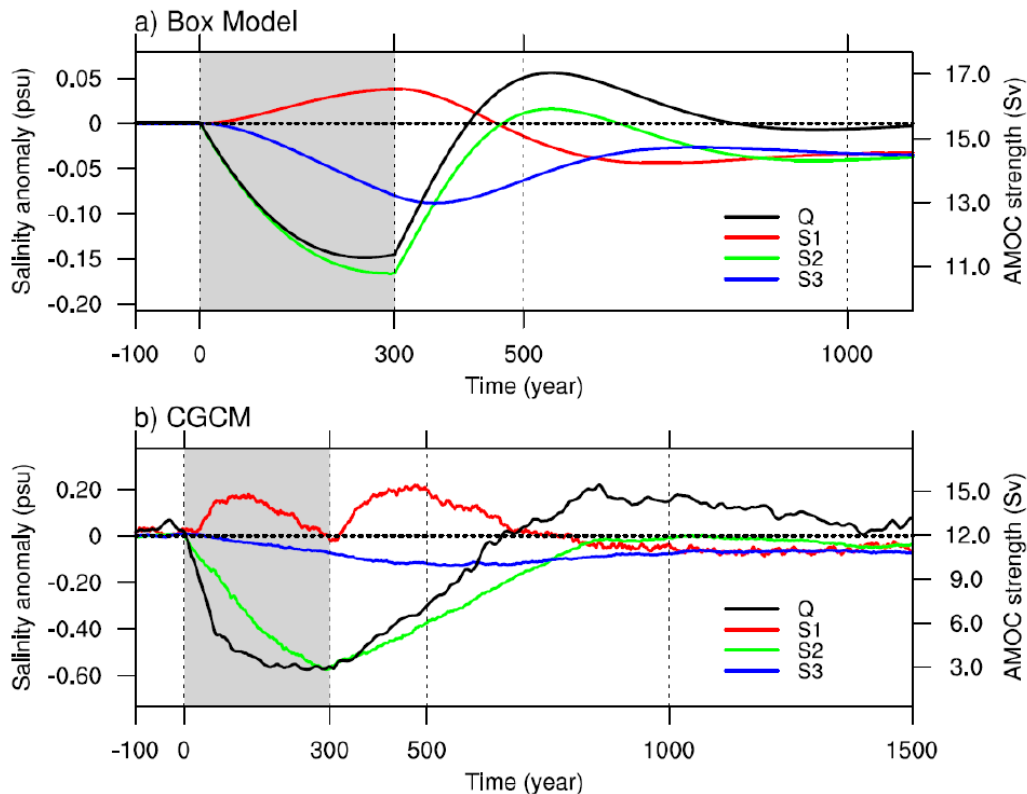
Fig.S7: Time series for AMOC transport (black) and box salinities, for an idealized hosing experiment in (a) a 3-box model and (b) the CCSM3 (salinity in ppt and transport in Sv.), illustrating a mechanism of AMOC overshoot associated with salinity adjustment. (see SOM, text 4 for more details). The box model is a hemispheric 3-box model, with a surface tropical box (box 1, red), a polar box from the surface to the bottom (box 2, green) and a deep tropical box (box 3, blue) (S9). The boxes are of equal latitudinal width for the tropical and polar boxes, and equal thickness for the surface and deep tropical boxes. A perturbation freshwater pulse is added into the polar box at a constant rate from t=1 to 300 years. The AMOC transport anomaly (black) decreases during hosing, and recovers subsequently, with an overshoot peak at t=520 years. In the recovery stage, the negative salinity anomaly recovers faster in the polar box (green) than in the deep tropical box (blue), generating an anomalous southward deep pressure gradient and therefore an overshoot of the AMOC. (b) Similar to the box model, but for an idealized hosing experiment in CCSM3 with the meltwater flux imposed over the North Atlantic at the constant rate of 33-mslv/1000-yr for 300 years on the glacial state (from 19 -18.7ka), The Atlantic basin is partitioned into box 1 ($45^{o}S - 20^{o}S$, 0-500-m), box 2 ($35^{o}N - 80^{o}N$, 0 − 2000-m) and box 3 ($45^{o}S - 20^{o}S$, 500 − 2000-m). Qualitatively, the evolution in CCSM3 seems to resemble that of the box model.

References for SOM

S1: W. D. Collins et al. *J. Climate,* **19,** 2122 (2006)

S2: S. G. Yeager, C. A. Shields, W. Large, J. Hack, *J. Climate*, **19**, 2545 (2003)

S3: B. L. Otto-Bliesner et al., *J. Clim.,* **19**, 2526 (2006)

S4: B. L. Otto-Bliesner et al., *Geophys. Res. Lett.,* **34,** L12707, doi:10.1029/2007GL029475 (2007).

S5: F. Joos, R. Spahni, *Proc Nat Aca Sci,* **105**, 1425, doi:10.1073/pnas.0707386105 (2008).

S6: W. R. Peltier, *Annu. Rev. Earth Planet. Sci*., **32**, 111 (2004)

S7: Z. Liu, M. Alexander, *Rev. Geophys*., **45**, RG2005, doi:10.1029/2005RG000172 (2007).

S8: P. U. Clark, N.G. Pisias, T.F. Stocker, A.J. Weaver, *Nature*, **415**, 863 (2002)

S9. H. Dijkstra, *Tellus*, **59A**, 695-705 (2007)

S10. S. Rahmstorf, *Nature*, **378**, 145 (1995).

S11. S. Rahmstorf, et al., *Geophys. Res. Lett*., L23605, doi:10.1029/2005GL023655 (2005)).

S12: A. Hu, B. L. Otto-Bliesner, G. A. Meehl and W. Han, *J. Climate*, **21**, 2239-2258 (2008)

S13: J. Mignot, A. Ganopolski, A. Levermann, *J. Clim*., **20**, 4884 (2007)

S14: E. Tzipermann, P. Ioannou, *J. Phys. Oceanogr*., **32**, 3427 (2002)

S15: E. Tzipermann, J. Toggweiler, Y. Feilks, K. Bryan, *J. Phys. Oceanogr*., **24**, 217 (1994)

SOM, BA_Science, Liu et al., revision2, 05/07/2009

S16: H. Stommel, *Tellus,* **13**, 224 (1961)

S17. J. F. McManus, R. Francois, J-M., Gherardi L. Keigwin , S. Brown-Leger, *Nature*, **428**, 834 (2004)

S18. J. Stanford et al., *Paleoceanography*, **21**, PA4103, doi:10.1029/2006PA001340 (2006)

S19: Y. Yokoyama, K. Lambeck, P. Deckker, P. Johnston, L. Keith Fifield, *Nature*, **406,**713 (2000)

S20: P. U. Clark, A.C. Mix, *Quat. Sci. Rev*., **21**, 1 (2002)

S21: W. Peltier, R. Fairbanks, *Quat. Sci. Rev*., **25**, 3322 (2006)

S22: E. Bard, F. Rostek, J-L Turon, S. Gandreau, *Science*, **289**, 1321 (2000)

S23: P. U. Clark et al., *Science*, **293**, 283 (2001)

S24: Z. Liu, Y. Wang, R. Gallimore, M. Notaro, I. C. Prentice, *Geophys. Res. Lett*., **33**, L22709, doi:10.1029/2006GL028062 (2006).

S25: R. Fairbanks, *Nature*, **342**, 637 (1989)

S26: T. Henebuth, K. Stattegger, P. Grootes, *Science*, **298**, 1033 (2000)

S27: A. J. Weaver,, O. A. Saenko, P. U. Clark, J. X. Mitrovica, *Science,* **299**, 1709 (2002)

S28: R. Stouffer, D. Dsidov, B. Haupt, *J. Climate*, **20**, 436 (2007)

S29: P. U. Clark et al., *Paleoceanography*, **11**, 563 (1996)

S30: T. Hanebuth, K. Stattegger, P.M. Grootes, *Science*, **288**, 1033 (2000)

S31: K.B. Cutler et al., *Earth Planet. Sci. Lett.*, **206**, 253 (2003)

S32: W. Peltier, G. Vettoretti, M. Stastna, *Geophys. Res. Lett*., **33** doi:10.1029/2005GL025251 (2006)

SOM, BA_Science, Liu et al., revision2, 05/07/2009

S33: D. Roche, H. Renssen, S. Weber, H. Goosse, *Geophys. Res. Lett.*, **34**, doi:10.1029/2007GL032064 (2007)

S34: A.E. Carlson, *Quat. Sci. Rev.*, **28**, in press (2009)